Bioactive Materials 45 (2025) 88–101

Contents lists available at ScienceDirect

Bioactive Materials

journal homepage: www.keaipublishing.com/en/journals/bioactive-materials

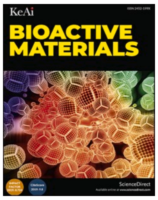

Bioinspired hierarchical porous tough adhesive to promote sealing of high-pressure bleeding

Yinghao Li [a,b,c,1], Dongling Xiao [a,b,c,1], Weixi Yan [a,b,c], Meilin Jiang [a,b,c], Ju Tan [a,b,c], Zhongliang Qin [a,b,d], Jingting Zhou [a,b,c], Yue Sun [a,b,c], Mingcan Yang [a,b,c], Guanyuan Yang [a,b,c], Yawei Gu [a,b,c], Yong Liu [a,b,d], Chuhong Zhu [a,b,c,*]

[a] *Department of Anatomy, Engineering Research Center for Organ Intelligent Biological Manufacturing of Chongqing, Key Lab for Biomechanics and Tissue Engineering of Chongqing, Third Military Medical University, Chongqing, 400038, China*
[b] *Engineering Research Center of Tissue and Organ Regeneration and Manufacturing, Ministry of Education, Chongqing, 400038, China*
[c] *State Key Laboratory of Trauma and Chemical Poisoning, Chongqing, 400038, China*
[d] *Zhong Zhi Yi Gu Research Institute, Chongqing Jiukang Medical Research Institute Co., Ltd., China*

ARTICLE INFO

Keywords:
Uncontrolled hemorrhage
Bio-inspired phase separation
Hierarchical porosity
Aggregate-based matrix
Tissue-conformable tough adhesion

ABSTRACT

Timely and stable sealing of uncontrolled high-pressure hemorrhage in emergency situations outside surgical units remains a major clinical challenge, contributing to the high mortality rate associated with trauma. The currently widely used hemostatic bioadhesives are ineffective for hemorrhage from major arteries and the heart due to the absence of biologically compatible flexible structures capable of simultaneously ensuring conformal tough adhesion and biomechanical support. Here, inspired by the principle of chromatin assembly, we present a tissue-conformable tough matrix for robust sealing of severe bleeding. This hierarchical matrix is fabricated through a phase separation process, which involves the in-situ formation of nanoporous aggregates within a microporous double-network (DN) matrix. The dispersed aggregates disrupt the rigid physical crosslinking of the original DN matrix and function as a dissipative component, enabling the aggregate-based DN (aggDN) matrix to efficiently dissipate energy during stress and achieve improved conformal attachment to soft tissues. Subsequently, pre-activated bridging polymers facilitate rapid interfacial bonding between the matrix and tissue surfaces. They synergistically withstand considerable hydraulic pressure of approximately 700 mmHg and demonstrate exceptional tissue adhesion and sealing in rat cardiac and canine aortic hemorrhages, outperforming the commercially available bioadhesives. Our findings present a promising biomimetic strategy for engineering biomechanically compatible and tough adhesive hydrogels, facilitating prompt and effective treatment of hemorrhagic wounds.

1. Introduction

Uncontrolled hemorrhage of soft tissues is a major cause of trauma-related fatalities globally [1,2]. While sutures and staples remain the mainstay of surgical hemostasis, timely and effective wound closure in emergency situations lacking surgical units presents a significant challenge [3]. Bioadhesive hydrogels offer a promising alternative due to their ease of use, low cytotoxicity, wet adhesion, and minimal tissue damage [4]. However, most clinically available hydrogels suffer from brittle matrix and weak tissue adhesion, limiting their effectiveness in diverse hemorrhagic scenarios [5]. Research efforts have focused on improving interfacial bonding while preventing cohesive failure [6], employing strategies such as photocuring [5,7–10], catechol-based chemistries [11–15], double-network (DN) architectures [16–20], and double-sided tape designs [21–23]. Despite these advancements, the biomechanical mismatch between hydrogel matrices and soft tissues

---

Peer review under responsibility of KeAi Communications Co., Ltd.

[*] Corresponding author. Department of Anatomy, Engineering Research Center for Organ Intelligent Biological Manufacturing of Chongqing, Key Lab for Biomechanics and Tissue Engineering of Chongqing, Third Military Medical University, Chongqing, 400038, China.

E-mail address: zhuch99@tmmu.edu.cn (C. Zhu).

[1] These authors contributed equally to this work.

https://doi.org/10.1016/j.bioactmat.2024.11.003
Received 31 July 2024; Received in revised form 3 November 2024; Accepted 3 November 2024

remains largely unaddressed. Especially in cases of heavy bleeding in dynamic tissues, such as arteries and hearts, the mechanical mismatch of adhesives can result in non-conformal contact with tissues in the early stages, potentially affecting the hemostatic effect [24]. Furthermore, it can disrupt normal systolic and diastolic function, ultimately compromising treatment outcomes [25]. Therefore, the development of effective strategies to overcome this biomechanical mismatch is urgently needed.

Various natural organisms, including mussels [26,27], geckos [28], sandcastle worms [29], tree frogs [30], clingfish [31], andrias davidianus [32,33], and barnacles [34,35], have inspired the development of adhesive materials by incorporating their diverse structures and compositions. Recently, extensive research has been conducted to imitate the inherent mechanical properties of biological tissues by integrating aggregated structures into hydrogel networks [36,37]. This incorporation creates a hierarchical porous structure, endowing the hydrogel matrix with versatile and robust mechanical properties, including high stiffness, strength, toughness, stretchability, and fatigue resistance [38–42]. These aggregates, formed through hydrophobic associations or hydrogen bonds, act as sacrificial structures during matrix deformation. This approach offers a viable solution for designing and constructing adhesive matrices that match the mechanical properties of cardiovascular tissues. However, in the case of rigid matrices, the introduction of external aggregates could potentially further increase stiffness, resulting in mechanical properties that are incompatible with those of soft tissues. Hence, the formation of aggregates in situ to induce the remodeling of the rigid network shows potential for creating a flexible yet robust adhesive matrix.

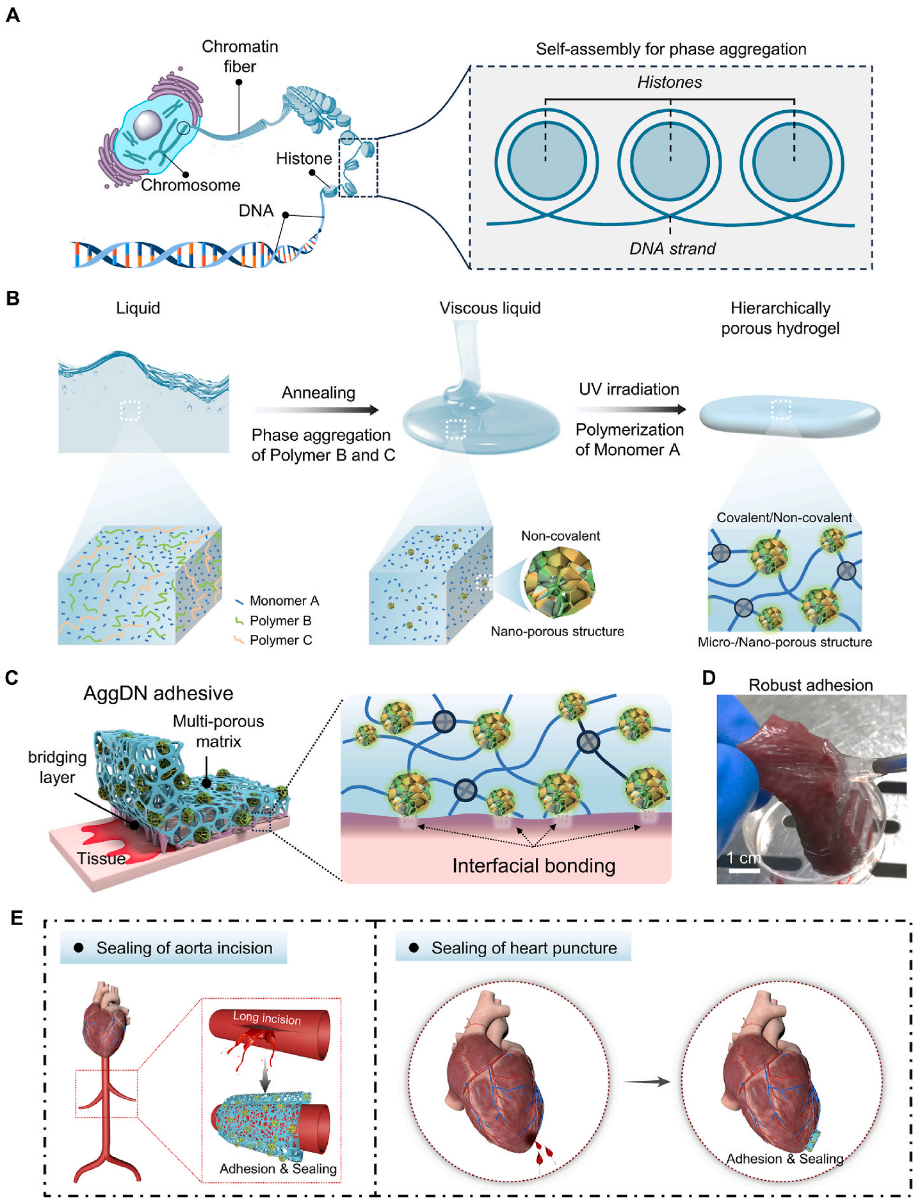

Fig. 1. Bioinspired design of a highly tough adhesive hydrogel. (A) Chromosomes consisting of DNA-histone protein aggregates present a compact shape, which resemble an adaptive hydrogel that can contract and expand in living cells. (B) Phase separation-assisted photo-polymerization procedure of the aggDN hydrogel. Nano-porous structure and micro-porous structure formation during the annealing and UV irradiation fabrication process, respectively. Monomer A: N-HEAA; Polymer B: agar; Polymer C: PLL. (C) Design of bioinspired aggDN adhesive hydrogels, consisting of a hierarchically porous matrix (aquamarine and orange-yellow) and a bridging adhesive polymer (magenta) that anchors firmly on blood-exposed tissue surfaces. (D) Photograph demonstrating the strong adhesion achieved between biological soft tissues (represented by porcine liver) and the engineered aggDN hydrogel, capable of withstanding significant deformation. (E) Schematic illustrations showcasing the application of aggDN adhesive hydrogels for the sealing of uncontrollable bleeding from aorta incisions and heart punctures.

Intracellular biomolecules like DNA, RNA, and proteins can form either bulk aggregates or dispersed microaggregates due to non-covalent interactions such as hydrogen bonds, electrostatic forces, hydrophobic effects, and van der Waals forces [43,44]. This aggregation results in phase separation. Stable, uniformly dispersed microaggregates are crucial for constructing hierarchical porous structures. Chromosomes serve as a representative example of such stable dispersed aggregates. They are formed through the electrostatic self-assembly of negatively charged DNA and positively charged histones, followed by a process of phase separation [45]. The resulting aggregate structure exhibits contraction and expansion behaviors similar to an adaptive hydrogel (Fig. 1A) [46].

Inspired by this, here we present a hierarchical porous tough matrix fabricated through an in-situ phase separation strategy. This matrix involves the formation of dispersed microaggregates within a rigid DN hydrogel, composed of an agar hydrogen bond network and a poly(N-hydroxyethyl acrylamide) (pHEAA) covalent network [47]. As shown in Fig. 1B, during the heat-cooling process, the introduction of polylysine (PLL) inhibits the formation of the agar-agar intramolecular hydrogen bond network. Instead, PLL self-assembles with agar to form numerous dispersed microaggregates in situ. Subsequently, photo-crosslinking leads to the creation of an aggregate-based double network (aggDN) matrix, achieving both structural and mechanical remodeling. Correspondingly, the presence of aggregate structures can disrupt the rigid physical crosslinking of the original network and incorporate newly formed noncovalent bond as mechanical relaxation and energy dissipation sites. The aggDN matrix exhibits an elastic modulus comparable to biological tissues, while simultaneously demonstrating exceptional flexibility and toughness. This enables conformable interaction with soft tissues via energy dissipation. To ensure robust interfacial bonding, a bridging adhesive layer was created by employing a negatively charged polymer grafted with cleavable N-hydroxysuccinimide (NHS) ester. This bridging layer efficiently promotes the sequential formation of both physical and covalent crosslinks between the surfaces of the matrix and the tissue (Fig. 1C). Finally, the aggDN adhesive hydrogel achieves fast and strong adhesion to various soft tissues (Fig. 1D). In an in vivo subcutaneous implantation model, the aggDN adhesive hydrogel shows favorable biocompatibility and biodegradability. Furthermore, we have demonstrated its excellent hemostatic and reparative capabilities in animal models of cardiac hemorrhages in rats and aortic hemorrhages in canines (Fig. 1E). In comparison, the clinically available hemostatic counterparts have shown limited efficacy in addressing such critical emergency situations.

2. Materials and methods

2.1. Materials

N-(2-Hydroxyethyl)acrylamide (N-HEAA), agar (gel strength: 800–1000 g/cm^2), and polylysine hydrochloride (PLL) were purchased from Aladdin Biochemical Technology Co., Ltd. (Shanghai, China). Cyanoacrylate adhesives were purchased from Taikoboman Medical Technology Co., Ltd. (Hubei, China). Porcine fibrin sealant was purchased from Bioseal Biotech Co., Ltd. (Guangzhou, China). Sodium hyaluronate (Mw = 40000) was purchased from Bloomage Biotech Co., Ltd. (Shandong, China). Phosphate buffer saline (PBS) solutions (100 mM, pH 7.0–7.4) were prepared in-house. Ultrapure water with a specific resistance of 18.2 MΩ at 25 °C was generated by a Mili-Q Integral 3 (Millipore) ultrapure water purification system. Other reagents were obtained from commercial sources and used without further purification.

2.2. Fabrication of adhesive hydrogels

2.2.1. Preparation of hydrogel matrix

To create the pHEAA/agar/PLL (aggDN) hydrogel matrix, a one-pot heating-cooling and photopolymerization method was used. The process involved mixing 40 wt% N-HEAA, 5 wt% agar, 2 wt% PLL, and 0.4 wt% Irgacure 2959 (I2959) in nitrogen-purged deionized water, heating and stirring at 95 °C for 20 min, and then casting into a glass mold. After cooling to room temperature, the gel was photopolymerized under UV light (365 nm, 48 W) for 30 min. Similar methods were used to prepare pHEAA/agar (DN) and pHEAA (SN) hydrogels. The hydrogels were stored at 4 °C until use. To optimize the aggDN matrix, the effects of varying PLL concentrations (1–5 wt%) on the mechanical properties were evaluated (Supplementary Table 1).

2.2.2. Preparation and characterization of adhesive bridging polymer: hyaluronic acid N-hydroxysuccinimide (HA-NHS)

HA-NHS was prepared and characterized using previously described methods [48]. Initially, 1 g of hyaluronic acid (MW = 40 kD) was dissolved in 20 mL of PBS (0.1 M, pH 7.4), followed by the addition of 1.43 g of 1-ethyl-3-(3-diemthylaminopropyl) carbodiimide•HCl (EDC•HCl) and 1.6 g of N-hydroxysuccinimide (NHS). The mixture was stirred at room temperature for 2 h, cooled to −20 °C, and then precipitated with cold ethanol. The resulting white precipitate was collected via centrifugation, washed, and dried under vacuum for 24 h before storage at −20 °C. The degree of NHS substitution was determined using ^{1}H NMR spectroscopy, analyzing the hydrogen integration of the methylene groups ($\delta = 2.62$ ppm, 4H) of the succinimide ester relative to the methyl resonance of the acetamido group ($\delta = 1.95$ ppm, 3H) in the GlcNAc residues.

2.2.3. Formation of adhesive hydrogels

The HA-NHS dry powder was quickly dissolved in PBS (0.1M, pH 7.4) using vortexing, resulting a final concentration of 50 mg/mL. Subsequently, the bridging polymer solution was applied to the surface of hydrogel matrix (50 μL/cm^2) and then pressed onto the target tissues.

2.3. SEM characterization

To characterize the inner structure of adhesive hydrogels, all samples were subjected to freeze-drying and then immersed in a liquid nitrogen bath and fractured. The exposed interior of the samples was sputter-coated with platinum and subsequently transferred into a chamber for SEM (ZEISS crossbeam 340) analysis.

2.4. Fourier transform infrared (FT-IR) spectroscopy characterization

The functional groups present in adhesive hydrogels were characterized using FT-IR spectroscopy (Nicolet FT-IR iS5, Thermo Fisher). The freeze-dried samples were ground into powder and subsequently compressed with dried KBr. The FT-IR spectra were recorded across a wavenumber range of 4000 to 400 cm^{-1}. The raw curves in the 4000 to 2300 cm^{-1} region, corresponding to the -CH, -NH, and -OH groups, were deconvoluted into Gaussian components using a peak analyzer tool (Origin 8.1) based on a previously reported method [49,50]. To quantitatively understand the specific intra- and intermolecular interactions in the adhesive hydrogels, the areas of the peaks related to hydrogen bonds (-OH, -NH) were calculated. All data were fitted with r^2 values greater than 0.995.

2.5. UV–vis spectroscopy characterization

The transparency of hydrogel matrices formed through a heating-cooling process was quantitatively assessed using an UV–visible (UV–vis) spectrophotometer (model UV-4800, UNICO). Initially, the absorption spectra (Abs) of the samples were measured within the visible range of 370 nm–800 nm. Then, transmittance (T) was calculated using the following equation: $T = \frac{1}{10^{Abs}} \times 100\%$.

2.6. Rheological analysis

Rheological characterization of a heated-cooled matrix was performed using a TA DHR-1 rheometer at 37 °C. Viscosity and shear stress were determined via a flow test employing a logarithmic shear rate sweep (0.001–10 s^{-1}). Oscillatory tests, encompassing both a strain sweep (0.01–1000 % at 1 Hz) to assess the amplitude dependence of the storage (G') and loss (G'') moduli, and time sweeps (alternating 1 % and 100 % strain at 1 Hz with 250 s intervals), were conducted to evaluate the material's viscoelastic recovery.

2.7. Porosity measurement

The porosity of the prepared hydrogel matrices (SN, DN and aggDN) was evaluated according to previously reported method with a slight modification [51]. The samples were lyophilized and fractured for SEM characterization. In the SEM images, the black regions represent the pores formed within the matrices, while the white regions represent the matrices scaffold. Using ImageJ software, the area occupied by the black regions in pixels can be computed. The porosity can then be calculated using the following equation: Porosity = $(A_{\text{black}}/A_{\text{total}}) \times 100$ %. Where A_{black} denotes the pixel area occupied by the black regions; A_{total} denotes the total pixel area of the image. The porosity values are means ± SD (n = 4).

2.8. Swelling properties

The adhesive hydrogels (SN, DN, and aggDN) were fabricated using the mold and then lyophilized and weighed. Afterward, the samples were incubated in PBS at 37 °C for different durations (Day 1, 2, 3, 5, 10, 18). At each time point, the weights of the swollen samples were measured. The swelling ratio was calculated using the formula: Swelling ratio = $[(W_{\text{wet}}\text{-}W_{\text{dry}})/W_{\text{dry}}] \times 100$ %. Where W_{dry} is the dry weight of the initial sample and W_{wet} is the weight of sample after swelling. The values of swelling ratio are means ± SD (n = 4).

2.9. Stability in different solvents

The stability of the adhesive hydrogels was assessed in various solvents known to break hydrogen bonds. The samples were immersed in water, a 5 M urea solution, or a 5 M NaSCN solution at room temperature. Subsequently, the changes in appearance and micro-morphology were documented through photographs taken at different time intervals (1 h, 24 h).

2.10. Mechanical characterization

2.10.1. Uniaxial tensile test

Dumbbell-shaped hydrogel specimens (20 mm length, 10 mm gauge width, 0.8 mm thickness) were tensile-tested using a ZhiQu mechanical tester (50-N load cell) at strain rates of 10 or 50 mm/min. Stress and strain were calculated from force-extension data, using the initial cross-sectional area and clamp distance (5 mm), respectively. Three replicates were tested per experimental group.

For the tensile tests, the ultimate tensile stress and strain were measured at the point of failure. Bulk toughness was determined by calculating the area under the stress-strain curve to rupture [42], and elastic moduli were calculated from the slope of the stress-strain curve at strains below 15 %.

For the stress-relaxation test, the samples were stretched to 100 % strain and the subsequent stress decay over time was recorded. The stress values were normalized to the initial stress for consistency. The stress-relaxation curve was fitted using a generalized Maxwell-Wiechert four-component model consisting of a linear spring in parallel with three dashpots [52]. The model is given by the equation: $\sigma(t) = \sigma_0 + \sum_{i=1}^{3} \sigma_i e^{-t/\tau_i}$, where $\sigma(t)$ is the normalized stress, σ_0 is the normalized constant stress of the spring, σ_i is the normalized stress of the dashpots, and τ_i are the characteristic relaxation time constants. Nonlinear curve fitting was performed using Origin 8.1, resulting in the determination of the elastic component (σ_0) and the decay half time ($\tau_{1/2}$).

For the hysteresis test, the samples were initially loaded to a strain of 100 % and then unloaded back to the initial state, both at a constant strain rate of 10 mm/min. By recording the stress-strain curves, the energy dissipated per unit volume of each sample was determined by calculating the area enclosed between the loading and unloading curves.

2.10.2. Pure shear test

Rectangular hydrogel samples (20 mm × 10 mm x 0.8 mm) with and without a 4 mm central notch were subjected to tensile tests at 50 mm/min. The critical crack length (L_c) between the clamps was determined when the notch turned into a running crack under tensile stress. Fracture energy (Γ) was determined by integrating the force-extension curve up to L_c for unnotched samples, calculating the work done ($U(L) = \int_0^{L_c - L_0} F\delta L$), and then normalizing by the sample's cross-sectional area (BC), yielding $\Gamma = U(L)/(BC)$.

2.11. Adhesion measurement

2.11.1. Interfacial toughness

The interfacial toughness between hydrogel and tissue samples was evaluated using the 180-degree peel test (ASTM F2256) on a universal mechanical test machine (ZhiQu, 50-N loading cell). The peeling speed was set at 50 mm/min. Both the hydrogel and tissue samples were prepared in a rectangular shape, measuring 20 mm in length and 10 mm in width. The interfacial toughness was calculated as twice the plateau force in the steady-state peeling region, divided by the hydrogel width. To support samples with low mechanical strength, poly(methyl methacrylate) films were applied by adhering them to the samples.

2.11.2. Burst pressure test

The burst pressures of the aggDN adhesive hydrogel and commercially available sealants (Bioseal and CA) were evaluated using the standard burst pressure test (ASTM F2392-04) on a custom-made burst pressure apparatus. Porcine skin samples were treated with 1 mol/L NaOH solution to remove fat, and a 3 mm hole was created. The hole was sealed with either a 10 × 10 × 0.8 mm aggDN hydrogel matrix or 200 μL of Bioseal or CA adhesive. After bonding, burst pressure was measured by pumping PBS at 0.75 mL/min and recording the pressure over time using a digital manometer.

2.12. In vitro cytocompatibility

The cytocompatibility of the aggDN adhesive hydrogel was assessed in vitro using a live/dead assay (ScienCell). HUVECs were treated for 24 h with conditioned medium from the aggDN adhesive hydrogel (80 mg of aggDN matrix and 8 μL of 5 % w/v HA-NHS incubated in 5 mL DMEM with 10 % FBS for 24 h) or control DMEM (10 % FBS). Cell viability, quantified via ImageJ analysis of fluorescent microscopy images (Evos FL Auto), was compared between the hydrogel-conditioned and control media.

2.13. In vitro degradation

In vitro degradation tests of adhesive hydrogels (SN, DN, and aggDN) were performed by shaping samples into small cylinders, lyophilizing, and then immersing them in PBS at 37 °C with shaking at 80 rpm. At designated time points, swollen samples were removed, rinsed with deionized water, lyophilized, and weighed again. The mass change was calculated using the formula: $(W_D/W_0) \times 100$ %, where W_0 is the initial dry weight and W_D is the weight after degradation (n = 4). This method allows for the determination of degradation kinetics over time.

2.14. Animal experiments

All animal experiments were conducted in compliance with ethical regulations for research involving animals and were approved by the Ethics Committee of the Third Military Medical University, China.

2.15. In vivo biocompatibility evaluation of aggDN adhesive hydrogel

The aggDN adhesive hydrogel was prepared aseptically, sterilized with UV light for 3 h, and implanted subcutaneously in male Sprague Dawley rats weighing 200–250 g. The rats were anesthetized with 1–1.5 % isoflurane, and 1.5 cm incisions were made on their dorsum to create subcutaneous pockets where 30–60 mg of the hydrogel was implanted. The incisions were closed with sutures. The animals were euthanized on days 3, 7, 14, 28, and 56 (n = 4), and the implants with surrounding tissue were explanted and fixed in 4 % paraformaldehyde for 24 h for subsequent histological and immunofluorescence analyses.

2.16. In vivo application of aggDN adhesive hydrogel in a rat cardiac puncture model

The sealing performance of aggDN adhesive hydrogel was evaluated in comparison to other commercial sealants for heart lesions in rats. Under anesthesia with 1.0–1.5 % isoflurane and mechanical ventilation, a left lateral thoracotomy was performed, and a ventricular puncture was made using a 2 mm diameter biopsy punch. A 3 mm diameter aggDN tough matrix with an adhesive layer was applied immediately to achieve hemostatic sealing, while other adhesives like CA or Bioseal (50 μL) were also tested. Bleeding was quantified within 5 min post-procedure. Cardiac function was assessed using echocardiography (VINNO 6 LAB, VINNO) before injury (day 0) and on days 3 and 14 after the injury and hemostatic sealing. Rat survival was monitored throughout the study. On days 1, 3, and 14, animals were euthanized, and hearts with implants were fixed in 4 % paraformaldehyde for histological and immunofluorescence analyses.

2.17. In vivo application of aggDN adhesive hydrogel in a canine aorta injury model

Anesthesia of Beagles (n = 3) was induced using pentobarbital sodium (1 %) and maintained by administering 2.0–2.5 % isoflurane via inhalation. The aorta was exposed and clamped, and a 5 mm incision was made. The aggDN tough matrix (5 × 1 × 0.8 mm) and other bioadhesives like CA (200 μL) or Bioseal (2 mL) were tested for hemostasis. After releasing the clamps 30–60 s later, bleeding was monitored. Blood flow was evaluated using ultrasound with color Doppler (Esaote Mylab system, Esaote) on days 14 and 28. The implants and surrounding tissue were excised, fixed in 4 % paraformaldehyde, and prepared for histological and immunofluorescence analyses.

2.18. Histology and immunohistology

The aggDN adhesive hydrogel and the surrounding tissue were subjected to histological analysis. The sections were fixed with 4 % paraformaldehyde overnight at 4 °C, and then processed for staining with H&E, Masson's trichrome, or immunofluorescence (Supplementary Table 2). For immunofluorescence staining, the following primary antibodies were used: Anti-CD3 for T-lymphocytes, Anti-CD68 for macrophages, anti-VEGF receptor 2 for endothelial cells, and anti-myosin heavy chain 4 for smooth muscle cells. The secondary antibodies used were goat anti-mouse IgG Alexa Fluor 488, goat anti-mouse IgG Alexa Fluor 594, and goat anti-rabbit IgG Alexa Fluor 594. Additionally, the sections were stained with Hoechst 33342 (Thermo Fisher) for visualizing the nuclei. The H&E-stained sections and immunofluorescence-stained sections were captured using an Olympus VS200 slide scanner.

2.19. Statistical analysis

Data were presented as mean ± SD. Statistical analysis was conducted using unpaired two-tailed Student's t-test for comparison between two groups or one-way analysis of variance (ANOVA) followed by Tukey's multiple comparison test for comparison between multiple groups. GraphPad Prism version 9 software was used for all statistical analyses.

3. Results and discussion

3.1. Fabrication and characterization of preliminary non-covalent physical networks through an annealing-initiated phase-separation process

The hierarchically porous structure was synthesized through successive annealing and photo-polymerization (Fig. 1B). For comparison, a single-network (SN) pHEAA hydrogel and a conventional DN pHEAA/agar hydrogel were also prepared. Initially, a hybrid HEAA-Agar-PLL non-covalent network was created via a heating-cooling (HC) process. After heating at 95 °C for about 20 min, the HEAA or HEAA/agar mixture turned into a transparent liquid (Fig. 2A). Conversely, the mixture of HEAA/agar/PLL became turbid and highly viscous upon the addition of PLL (Fig. 2A). Upon cooling, HEAA remained in a liquid state (SN^{HC}), while HEAA/agar formed a solidified, brittle hydrogel (DN^{HC}) (Fig. 2A and Supplementary Fig. 1A and B). In contrast, the HEAA/agar/PLL mixture produced a viscoelastic and cohesive gel ($aggDN^{HC}$) (Fig. 2A and Supplementary Fig. 1C). Microscopic analysis revealed aggregates dispersed within the $aggDN^{HC}$, which reduced its transparency compared to SN^{HC} and DN^{HC} (Fig. 2B). This observation was supported by UV–vis spectrophotometer measurements of the hydrogels' transmittance (Fig. 2C and Supplementary Fig. 2).

We characterized the rheological property of the SN^{HC} and $aggDN^{HC}$ by the flow and oscillatory tests (Fig. 2D–F and Supplementary Fig. 3). Flow tests revealed that the $aggDN^{HC}$ hydrogel exhibited shear-thinning behavior (Fig. 2D). Oscillatory amplitude sweep tests showed a constant storage (G') and loss (G'') modulus of $aggDN^{HC}$ at low deformations, followed by a sharp decrease at higher deformations, indicating yield behavior (Fig. 2E). The yield strain (Fig. 2E) and stress (Fig. 2F and Supplementary Fig. 3) were determined from these curves. The distinct yielding behavior of $aggDN^{HC}$, compared to DN^{HC}, highlights the significant impact of PLL on the network interactions, consistent with its observed shear-thinning properties. During the amplitude oscillatory time sweeping, the alternate strain cycling test (1 % or 100 % strain) was performed and the resulting moduli were obtained (Fig. 2G). The rheological property of $aggDN^{HC}$ switches between the solid-like behavior ($G' > G''$) at low strain and the liquid-like behavior ($G''> G'$) at high strain. Under high strain conditions, both G' and G'' decreased significantly, indicating physical dissociation of the cross-linked network. However, upon removal of the high strain, the network rapidly recovered its solid-like behavior, demonstrating self-healing properties. This contrasts with DN^{HC}, which was unable to reconstruct its network after high strain deformation (Supplementary Fig. 1B).

To examine the impact of hydrogen bonds on the stability of gel networks, we compared the dissolution of DN^{HC} and $aggDN^{HC}$ in different solvents at room temperature: water, 5 M urea, and 5 M NaSCN (Fig. 2H). Urea and NaSCN are common hydrogen-bond breaking agents, with NaSCN being more effective. After immersing DN^{HC} or $aggDN^{HC}$ in the selected solvent for 1 h, we observed that DN^{HC} remained insoluble and barely swollen in water and urea, yet fully dissolved in NaSCN, suggesting NaSCN could disrupt hydrogen bonds within the agar network of DN^{HC}. In contrast, $aggDN^{HC}$ formed microgels in water and urea solutions, with microgels being stable in water but somewhat degrading in urea. They were fully dissolved in NaSCN. These results indicate that the overall hydrogen bond network in DN^{HC} could

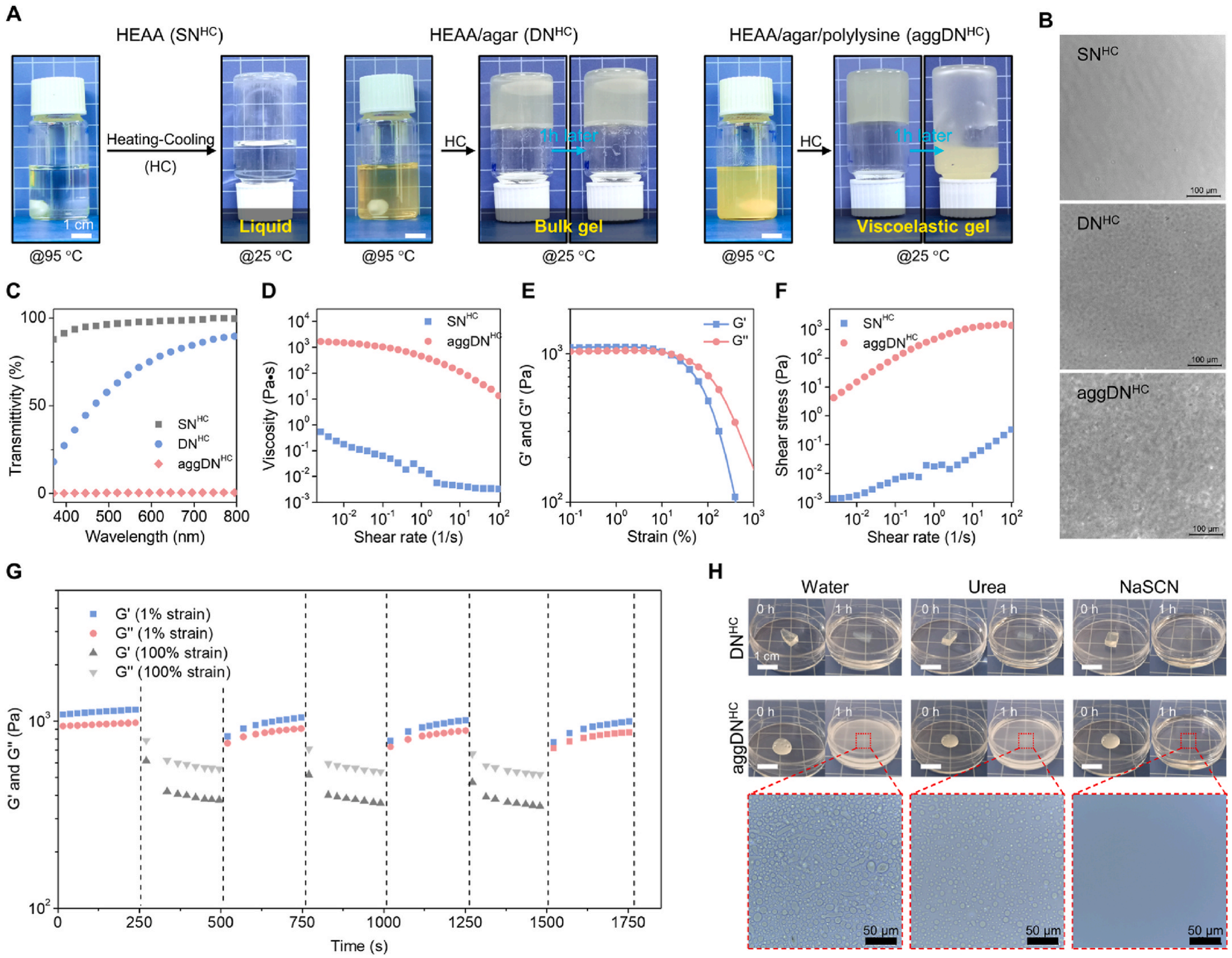

Fig. 2. Fabrication and physical properties of the aggDN hydrogel with hierarchically porous structure. (A) The gelation behaviors of the SN^{HC}, DN^{HC}, and $aggDN^{HC}$ during heating-cooling procedure. After cooling down to 25 °C, all of them were determined using a test tube inverting method, and the images were taken immediately for the SN^{HC}, DN^{HC}, and $aggDN^{HC}$ and 1 h later for DN^{HC} and $aggDN^{HC}$. (B) Photographs of the SN^{HC}, DN^{HC}, and $aggDN^{HC}$ measured by light microscope. (C) The transmittance spectra of the SN^{HC}, DN^{HC}, and $aggDN^{HC}$. (D) Viscosity of the SN^{HC} and $aggDN^{HC}$ in shear rate sweeping test. (E) Storage modulus (G') and loss modulus (G'') of the $aggDN^{HC}$ in strain sweeping test. (F) Shear stress of the SN^{HC} and $aggDN^{HC}$ in shear rate sweeping test. (G) Moduli of the $aggDN^{HC}$ under dynamic strain cyclic conditions (100 % strain and 1 % strain). (H) Comparison of the dissolution in water, urea (5M) and NaSCN (5M) for the DN^{HC} (up) and $aggDN^{HC}$ (down) at room temperature.

be broken into localized hydrogen bonds in $aggDN^{HC}$ due to the introduction of PLL. Additionally, the reformed intermolecular hydrogen bond networks, formed microphase aggregates, provided flexibility and ensure gel stability to some extent.

3.2. Fabrication and characterization of secondary covalent physical networks through photo-polymerization

The recoverable energy dissipation in hydrogels mainly originates from non-covalent crosslinking, while mechanical properties (elasticity, toughness, stability) are primarily attributed to covalent crosslinking. Therefore, the physically crosslinked SN^{HC}, DN^{HC}, and $aggDN^{HC}$ were photopolymerized into SN, DN, and aggDN hydrogels, respectively (Fig. 3A). SN and DN hydrogels were transparent, while aggDN was opaque (Fig. 3B), mirroring their pre-polymerization appearance. SEM imaging of cryo-fractured hydrogels revealed sponge-like porous structures (Fig. 3B). SN exhibited a micrometer-scale network (~10 μm pores), consistent with its purely covalent structure. DN showed a smaller pore size (~5 μm) due to its interpenetrating covalent/non-covalent network. AggDN, however, displayed island-like aggregates with nanoporous structures within the network. With the increase in PLL concentration, the microscopic structure of aggDN transitions from micro-pores to nano-pores (Supplementary Fig. 4). Porosity measurements further substantiated these observations (Fig. 3C): SN (48.0 ± 2.4 %), DN (43.4 ± 2.1 %), and aggDN (29.2 ± 2.5 %). The reduced porosity in aggDN can be attributed to the formation of dispersed aggregates.

Fourier transform infrared (FT-IR) spectroscopy is crucial for understanding hydrogen bonding interactions in biopolymers [49,50]. By applying FT-IR analysis, we qualitatively and quantitatively examined the structural differences of various hydrogel matrices at the molecular level. The FT-IR spectra of SN, DN, and aggDN showed distinct features in the functional group region (4000 cm^{-1}–2300 cm^{-1}) (Supplementary Fig. 5A). After deconvolution, six specific absorption bands were identified, including three hydrogen bond-related bands (Supplementary Fig. 5B–D). SN exhibited a moderate band at 3559 cm^{-1} for free O-H stretching, a large band at 3291 cm^{-1} for overlapped stretching vibration of N-H of secondary amide and intramolecular O-H, and a broad band at 2887 cm^{-1} for intermolecular O-H stretching (Supplementary Fig. 5B).

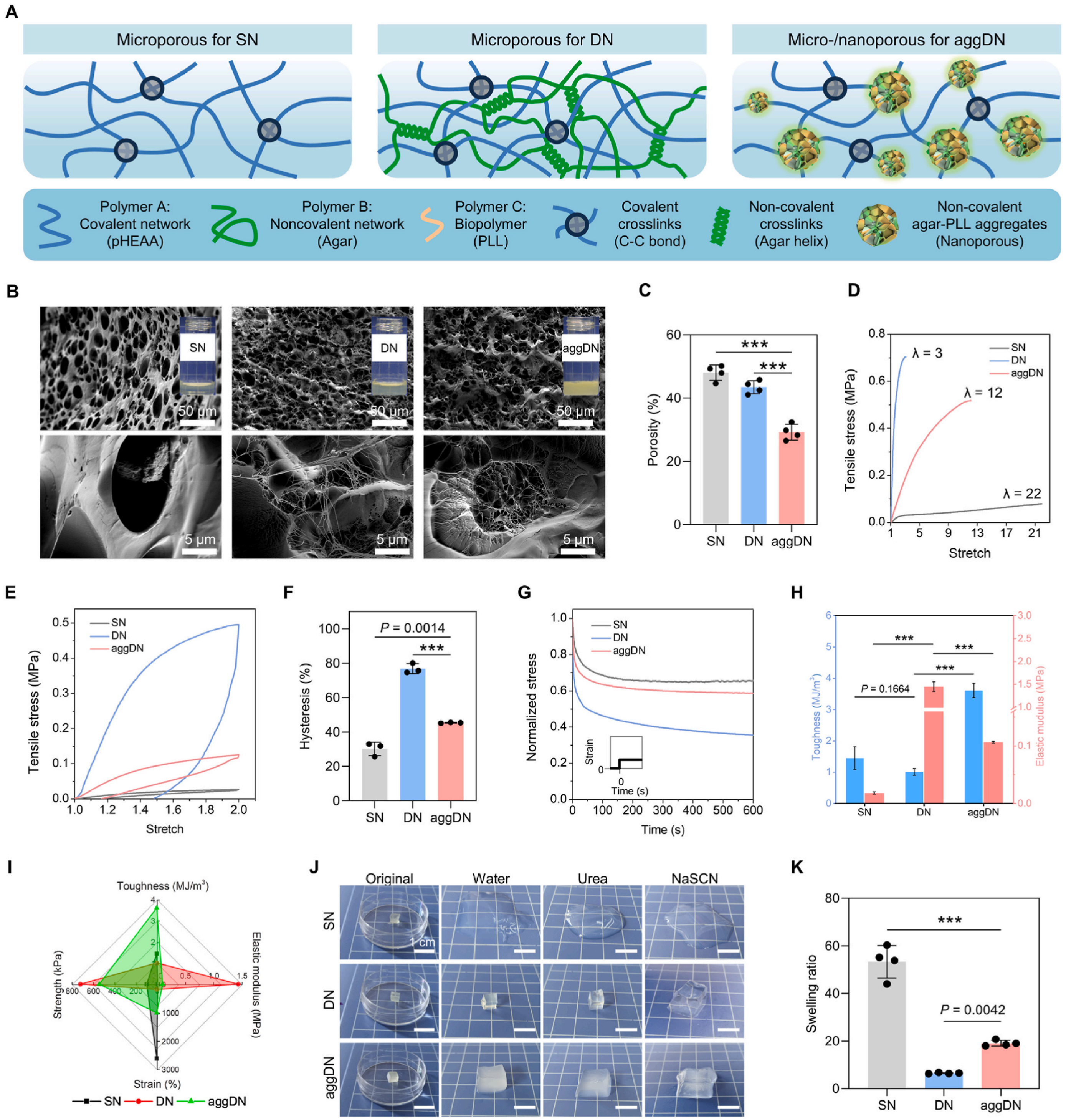

Fig. 3. Physical characterization of various hydrogel matrices. (A) Schematic illustrations of the microscopic structures for SN, DN, and aggDN matrices. In aggDN, PLL (orange chains) unwinds most of agar's (green chains) rigid hydrogen-bond networks, and the newly formed PLL-agar aggregates intertwine with covalent pHEAAs (blue networks) to create a soft and tough hydrogel matrix. (B,C) SEM images (B) and porosity (C) of the SN, DN, and aggDN. (D) Tensile stress-stretch curves of the SN, DN, and aggDN, each of which stretched to break. (E) Uniaxial tensile loading-unloading curves of the SN, DN, and aggDN at stretching ratio of 2, just below the elongation at break of the DN. (F) Hysteresis of the SN, DN, and aggDN under uniaxial loading and unloading at stretching ratio of 2. (G) Stress relaxation curves of the SN, DN, and aggDN at $\lambda = 2$. (H) Tensile toughness and elastic modulus of the SN, DN, and aggDN. (I) A spider diagram quantitatively summarizes the mechanical properties of the SN, DN, and aggDN. (J) Photographs of the swelling behaviors of SN, DN, and aggDN hydrogels in various soaking solutions, including water, a 5 M urea solution, and a 5 M NaSCN solution, at room temperature for a duration of 24 h. (K) Swelling ratio of the SN, DN, and aggDN in PBS buffer for 24 h. Data in C, F, H, K represent mean ± SD (n = 3–4 per group). *P* values were determined by one-way ANOVA followed by Tukey's multiple comparison test (***$P \leq 0.001$).

Upon introducing agar into pHEAA to form DN, the intensity of the intermolecular O-H stretching band decreased significantly, indicating inhibited intermolecular hydrogen bonding (Supplementary Fig. 5C). In aggDN, formed by adding PLL to DN, the intensity of the intermolecular O-H stretching band recovered and even increased, suggesting the formation of new intermolecular hydrogen bonds related to aggregates between pHEAA, agar, and PLL (Supplementary Fig. 5D).

The diverse molecular compositions and interactions within these materials result in distinct mechanical properties (Fig. 3D–I, Supplementary Table 1, and Movie 1). SN exhibited an ultrahigh ultimate strain of λ = 22 but low ultimate tensile stress of 94.6 ± 13.9 kPa (Fig. 3D). Conversely, DN showed a high ultimate tensile strength of 721.1 ± 14.8 kPa but a lower ultimate strain, only three times the original length (Fig. 3D). Notably, the inclusion of PLL in suitable

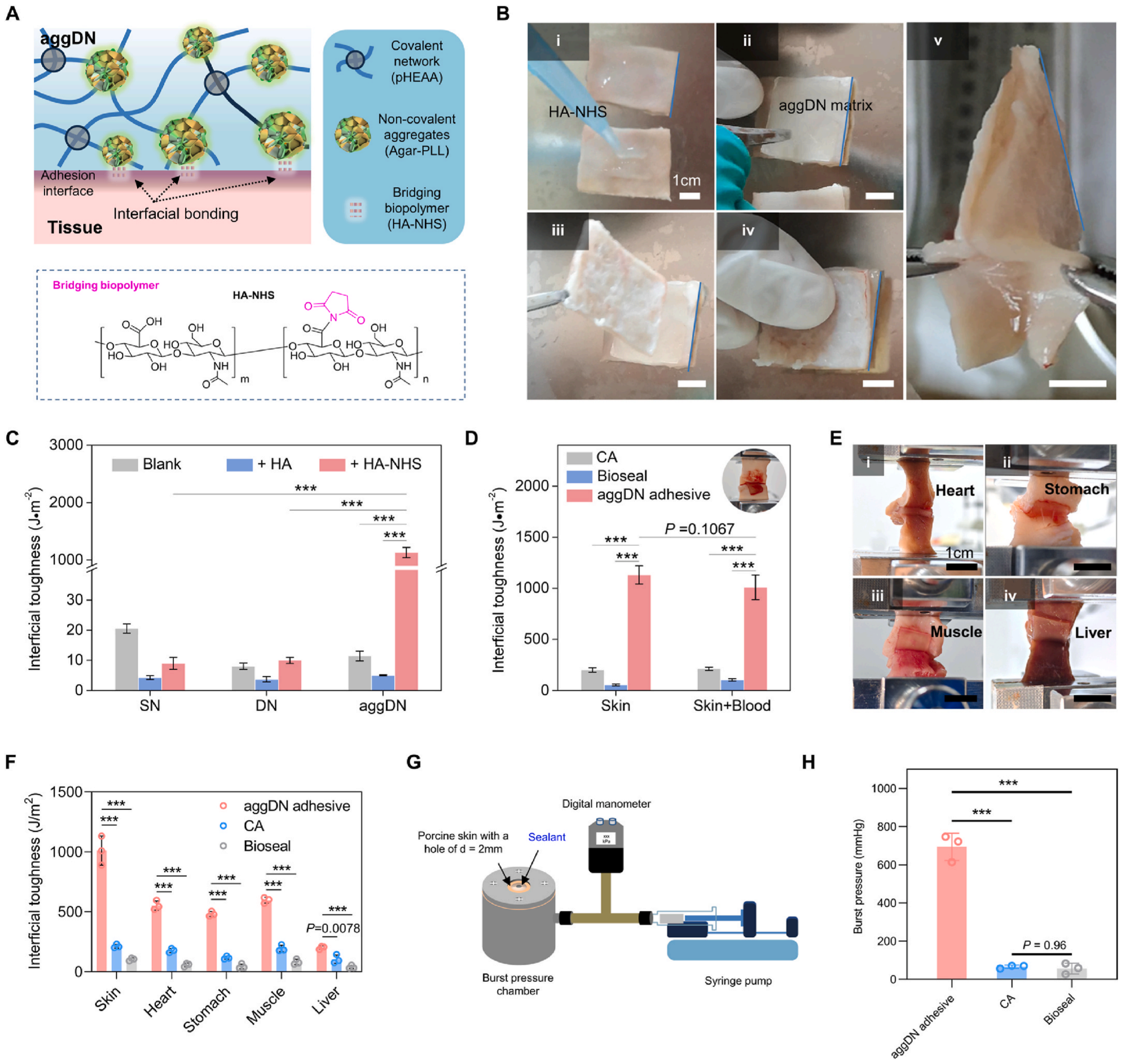

Fig. 4. In vitro adhesion performance and sealing ability. (A) Schematic illustration of the aggDN-based adhesive hydrogel, which consists of a dissipative aggDN matrix (aquamarine), and an adhesive bridging biopolymer HA-NHS. (B) In vitro evaluation for the adhesion of aggDN adhesive hydrogel on porcine skin. The process involves: (i) Applying a 5 % HA-NHS solution to the wet surface of two porcine skin pieces; (ii & iii) Placing an aggDN matrix between the skin pieces; (iv) Gently pressing for 10 s to create the adhesive bond; (v) Achieving robust tissue adhesion. (C) The adhesion strength of the SN, DN, and aggDN with different adhesive element on porcine skin. (D) Comparison of the adhesion strength of the aggDN adhesive hydrogel versus that of commercially available sealants on porcine skin with and without blood coverage. (E) In vitro evaluation of adhesion on diverse biological tissues with blood coverage. (F) The adhesion strength of the aggDN adhesive and other clinically available sealants (CA & Bioseal) on various biological tissues with blood coverage. (G) Schematic illustration of standard setup for in vitro burst pressure test of a punctured porcine skin sealed by various sealants. (H) The average burst pressure of the aggDN adhesive hydrogel and commercially available sealants including CA and Bioseal. Data in C,D,F,H represent mean ± SD (n = 3 per group). *P* values were determined by one-way ANOVA followed by Tukey's multiple comparison test (****P* ≤ 0.001).

proportions resulted in optimized aggDN, displaying an exceptional combination of high ultimate stress (544.0 ± 43.5 kPa) and high ultimate strain ($\lambda = 12$) (Fig. 3D and Supplementary Fig. 6). To calculate the fracture energy of aggDN, both notched and unnotched samples were subjected to tensile stress at the same strain rate (Supplementary Fig. 7A and Movie 2). The multiple bonding network within aggDN effectively dissipated energy by stabilizing deformation and unzipping a wide crack, ultimately achieving a high fracture energy of 9170 J/m^2 (Supplementary Fig. 7B and C).

The mechanical viscoelasticity of hydrogels was evaluated through hysteresis and relaxation behavior. During relaxation, non-covalent bonds such as hydrogen bonds break, leading to a decrease in stress and providing insights into their contribution to the overall structure. Hysteresis, quantified by the area of the hysteresis loop at a stretching ratio of 2, was low for SN (30.2 ± 3.9 %) but significantly increased for DN (76.8 ± 2.9 %), then decreased upon PLL addition for aggDN (45.4 ± 0.3 %) (Fig. 3E and F). Stress relaxation measurements, fitted by a generalized Maxwell-Weichert four-component model [52], showed that SN had minimal relaxation (~34 %) with a half-time of 9.5 s, whereas DN had pronounced relaxation (~67 %) with a faster rate ($\tau_{1/2} = 4.0$ s) (Fig, 3G and Supplementary Fig. 8). AggDN exhibited intermediate relaxation (41 %) but a comparable relaxation rate ($\tau_{1/2} = 3.8$ s) to DN (Fig, 3G and Supplementary Fig. 8). These findings indicate that the hydrogen bond-based agar network in DN contributed significantly to energy dissipation. The presence of PLL disrupted the rigid agar network and further assembled with agar to form a hierarchical porous structure, leading to the highest toughness (3.6 ± 0.2 MJ/m^3) and tissue-matched elastic modulus (106.3 ± 1.7 kPa) of aggDN (Fig, 3H,I and Supplementary Fig. 9).

The hydrogels exhibited distinct swelling behaviors when immersed in hydrogen bond-breaking solvents like water, 5 M urea, and 5 M NaSCN for 24 h at room temperature (Fig. 3J). SN hydrogel showed significant swelling and transparency in all solutions, while DN hydrogel exhibited slight swelling in water and urea but enlarged notably in NaSCN solution. The aggDN hydrogel, however, displayed moderate swelling in water and urea, with decreased transparency, and did not swell significantly further in NaSCN solvent, suggesting a lesser proportion of strong hydrogen bonds than DN. In physiological solutions, all hydrogels showed rapid initial swelling followed by a slower phase, with SN demonstrating the highest swelling ratio (79.5 ± 3.6), DN the lowest ratio (7.1 ± 0.3), and aggDN a moderate ratio (25.8 ± 0.9) by day 18 (Fig. 3K and Supplementary Fig. 10). This indicates that aggDN, with its multiple networks formed by covalent crosslinking, polymer chain entanglement, and hydrogen bonds, possesses suitable structural stability, making it a promising candidate for tough and conformable adhesive matrix.

3.3. Adhesion performance and sealing ability on diverse biological tissues

In addition to the dissipative tough matrix, a tissue adhesion layer is required to achieve strong tissue adhesion (Fig. 4A). Dispersive NH$_2$-riched microphase aggregates originated from PLL could be as adhesive site for further bio-adhesion. We designed a biocompatible adhesive polymer, HA-NHS, which contains reactive NHS ester groups (Fig. 4A and Supplementary Fig. 11). When applied under pressure, HA-NHS forms a thin layer of mucus between the hydrogel matrix and wet tissues. The NHS ester groups rapidly react with amines on both the aggDN hydrogel and tissue surfaces for tough conformable adhesion.

The adhesion performance of hydrogels on wet tissues was initially assessed through standard mechanical tests in vitro. Interfacial toughness measurements were preferred to evaluate the adhesion strength and kinetics between bioadhesives and tissues [16,22]. Porcine skin was selected as a model tissue to demonstrate the bridging capability of HA-NHS. Its similarity to human skin and high tensile strength, compared to less robust tissues, ensured it could withstand the stresses of dragging during measurements. First, HA-NHS solution (5 wt%) as bridging polymer was applied to the wet surface of two pieces of porcine skin (Fig. 4B–i). By placing an aggDN matrix between the skin pieces (Fig. 4B, ii and iii) and gently pressing for 10 s (Fig. 4B–iv), the aggDN adhesive hydrogel achieves robust tissue adhesion (Fig. 4B–v, and Supplementary Movie 3). This adhesion strength exceeds 1000 J/m^2 within just 10 min (Fig. 4C). Subsequent comparisons showed that without adhesive layers, SN, DN, and aggDN matrices had low adhesion to porcine skin (Fig. 4C). Even with HA or HA-NHS as the adhesive layer, SN or DN hydrogels did not exhibit significantly improved adhesion, suggesting that exclusive non-covalent cross-linking is not sufficient for strong adhesion. In contrast, the flexibility of aggDN facilitated its conformal attachment to soft skin tissue. Under the entanglement and covalent bridging of HA-NHS, aggDN achieved strong tissue adhesion.

Compared to clinically available cyanoacrylate (CA) and fibrin glue (Bioseal), the aggDN adhesive hydrogel showed superior adhesion to porcine skin, even in the presence of interfacial water or blood (Fig. 4D–F). Both CA and Bioseal exhibited weak tissue adhesion. CA's adhesion was significantly impaired by water, a consequence of its rigid structure and compromised chemical bonding. The poor performance of Bioseal stemmed from its low toughness and reliance on non-covalent bonding, although the presence of blood slightly enhanced its adhesion. In contrast, aggDN adhesive hydrogel maintained high adhesion strength across various wet tissues and organs (skin: ~1100 J/m^2, heart: ~610 J/m^2, stomach: ~510 J/m^2, muscle: ~650 J/m^2, liver: ~210 J/m^2), unaffected by blood exposure (Fig. 4E and F, Supplementary Fig. 12 and Movie 4). The collective results indicated that aggDN adhesive hydrogel possesses both high toughness and strong tissue adhesion, making it suitable for hemostatic sealing. In vitro burst pressure tests, using a porcine skin model with a 2 mm hole, revealed a burst pressure of 694 ± 71 mmHg for aggDN adhesive hydrogel, significantly higher than human normal systolic blood pressure (120 mmHg) and that of commercially available CA and Bioseal (Fig. 4G and H, Supplementary Fig. 13, and Movie 5). The unique combination of high interfacial toughness and burst pressure exhibited by the aggDN adhesive hydrogel is unparalleled among existing tissue adhesives (Supplementary Fig. 14) [16,18,23], showcasing its exceptional wound sealing capabilities.

3.4. Biocompatibility and biodegradation study

To evaluate the biocompatibility and biodegradation of the aggDN adhesive hydrogel, both in vitro and in vivo assessments were conducted. Firstly, an in vitro cellular cytotoxicity study was carried out to assess its biocompatibility. As shown in Fig. 5A and B, human umbilical vein endothelial cells (HUVECs) maintained high viability and spread well in the aggDN adhesive hydrogel-conditioned medium after 24-h culture, which was comparable to that in the control medium. Furthermore, the aggDN adhesive hydrogel exhibited biodegradability under physiological conditions. Over a period of 18 days, the hydrogel mass gradually decreased to approximately 67 ± 3 % (Supplementary Fig. 15).

For the in vivo assessment of biocompatibility and biodegradability, the aggDN adhesive hydrogel and other commercial sealants were subcutaneously implanted in rats. Tissue samples containing the adhesive sealants were excised on days 3, 7, and 14 for histological analysis (Fig. 5C). Hematoxylin and eosin (H&E) staining revealed initial presence of inflammatory cells at the tissue interface, which subsequently infiltrated into the dense hydrogel network as aggDN matrix degraded by day 3. By day 7, the aggDN matrix had swollen, and the local inflammatory response had diminished. By day 14, non-inflammatory cell infiltration was observed within the aggDN matrix, accompanied by the formation of new fibrous tissues, while the aggDN matrix remained firmly adhered to adjacent tissues. In contrast, the commercially available sealant CA induced significant inflammation and tissue fibrosis (Supplementary Fig. 16). Another clinically used sealant (Bioseal) elicited a lower inflammatory response than CA but still higher than that caused by the aggDN adhesive hydrogel (Supplementary Fig. 16).

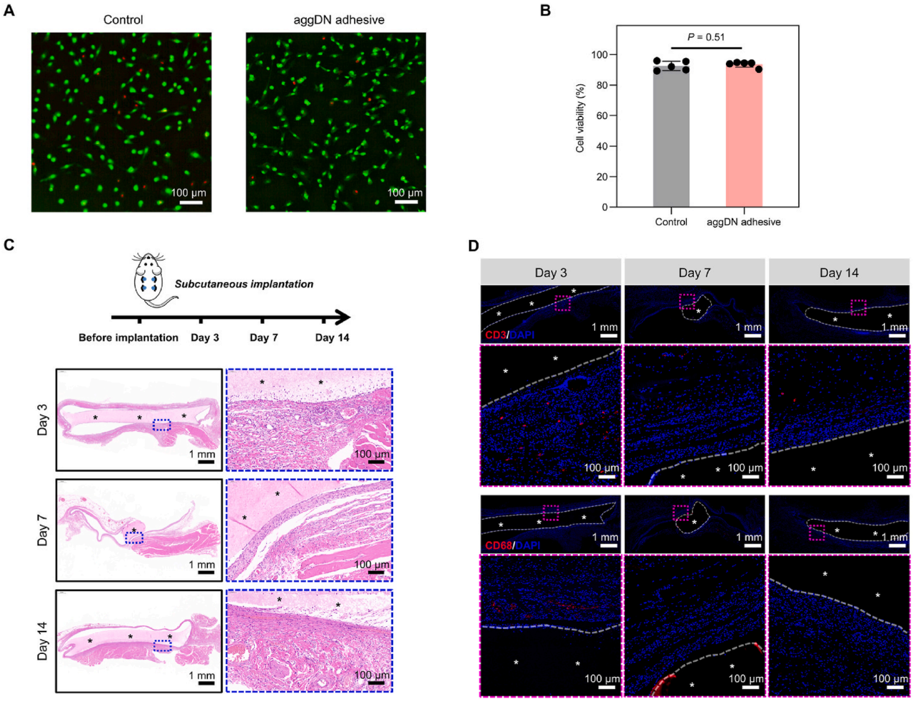

Fig. 5. Biocompatibility in vitro and in vivo. (A,B) Representative confocal microscopy images (A) and quantification of cell viability (B) of HUVECs in live/dead assays after 24 h culture in control media and aggDN adhesive hydrogel-incubated media. (C) Schematic and representative histological images of the aggDN adhesive hydrogel with surrounding tissues stained with H&E on days 3, 7, and 14 of subcutaneously post-implantation. (D) Representative immunofluorescence images of the aggDN adhesive hydrogel with surrounding tissues on days 3, 7, and 14 of subcutaneously post-implantation. Blue color represents the cell nuclei (DAPI), red color represents the lymphocytes (CD3, top) or macrophages (CD68, down). Within these images in C and D, the asterisk (*) marks the location of the implanted aggDN adhesive hydrogel. Data in B represent mean ± SD (n = 5 per group). *P* values were determined by unpaired two-tailed Student's t-test (****P* $\leq$ 0.001).

Immunohistological analysis was further conducted to study the local immune response (Fig. 5D and Supplementary Fig. 17). Immunofluorescence staining revealed the presence of $CD3^+$ lymphocytes and $CD68^+$ macrophages at the interface between the aggDN matrix and surrounding tissues on day 3, which diminished by days 7 and 14 (Fig. 5D and Supplementary Fig. 17). In contrast, both the CA and Bioseal groups exhibited significant infiltration of immune cells ($CD3^+$ and $CD68^+$) by day 3 after subcutaneous implantation. The numbers of lymphocytes and macrophages decreased by day 14 post-implantation but remained markedly higher compared to the aggDN group. Furthermore, the subcutaneous implantation of aggDN adhesive hydrogel in a rat model was extended to observe its in vivo degradation over time. Results indicated gradual degradation of aggDN starting approximately 14 days post-implantation, with significant degradation occurring between 28 and 56 days (Supplementary Fig. 18). Long-term degradation of aggDN in vivo is currently under observation. These findings demonstrate the biocompatibility, biodegradability, and minimal host response stimulated by the aggDN adhesive hydrogel in vivo.

3.5. In vivo evaluation of the sealing capacity in a rat cardiac puncture model

Based on the excellent sealing performance of aggDN in vitro, we further evaluated its hemostatic capability in a rat cardiac defect model (Fig. 6). The aggDN adhesive hydrogel was applied to treat hemorrhagic injuries on the ventricular wall, where constant heartbeats pose a significant challenge (Fig. 6A and Supplementary Movie 6). After making a 2 mm diameter cardiac puncture wound, we immediately delivered the aggDN adhesive hydrogel to the lesion site. Within 30 s, aggDN adhesive hydrogel adhered firmly on the lesion region and completely stopped the bleeding (Fig. 6A). In contrast, CA and Bioseal failed to achieve effective hemostasis in the same timeframe (Supplementary Fig. 19 and Supplementary Movie 7, 8). At day 14, the excised aggDN adhesive hydrogel-treated heart indicated that the adhesion between aggDN adhesive hydrogel and ventricular tissues still existed (Fig. 6B). We also conducted a thorough evaluation of the hemostatic ability of aggDN adhesive hydrogel by carefully measuring the amount of blood loss during the treatment within a 5-min period. As shown in Fig. 6C, there is nearly no blood loss for aggDN adhesive hydrogel-treated group compared to the control group and other commercially available sealant-treated groups. Even after 5 min, both the CA- and Bioseal-treated groups were unable to stop the bleeding. Furthermore, the aggDN adhesive hydrogel-treated group presents 100 % survival in 2 weeks, which reflects the best first-aid effect (Supplementary Fig. 20). Echocardiography measurements were performed to assess the cardiac function of operation group before and after aggDN adhesive hydrogel treatment (Fig. 6D–F). The results showed that the left ventricular ejection fraction (LVEF) and left ventricular fraction shortening (LVFS) of aggDN adhesive hydrogel-treated group maintained normal level. Histological analysis at day 1, 3, 14 indicated that aggDN adhesive hydrogel formed a tight adhesion to the lesion site of heart. With the degradation of aggDN networks and infiltration of normal cells, the soft tissue defects were gradually filled with regenerative fibrous tissue and got healed (Fig. 6G). There was also no significant collagen fibrosis at the lesion site of myocardium (Fig. 6H).

We also collected serum samples from rats at three time points: before surgery, 3 days post-surgery, and 14 days post-surgery, to assess levels of inflammatory markers (TNF-α, IL-6) and myocardial injury markers (cTnT, CK, CK-MB). The results indicated that inflammation had largely resolved by day 14 and myocardial injury had significantly recovered (Supplementary Fig. 21A–E). Additionally, heart rate returned to normal levels by day 14 post-surgery (Supplementary Fig. 21F). Furthermore, immunofluorescence analysis revealed a mild inflammatory response induced by the aggDN adhesive hydrogel around

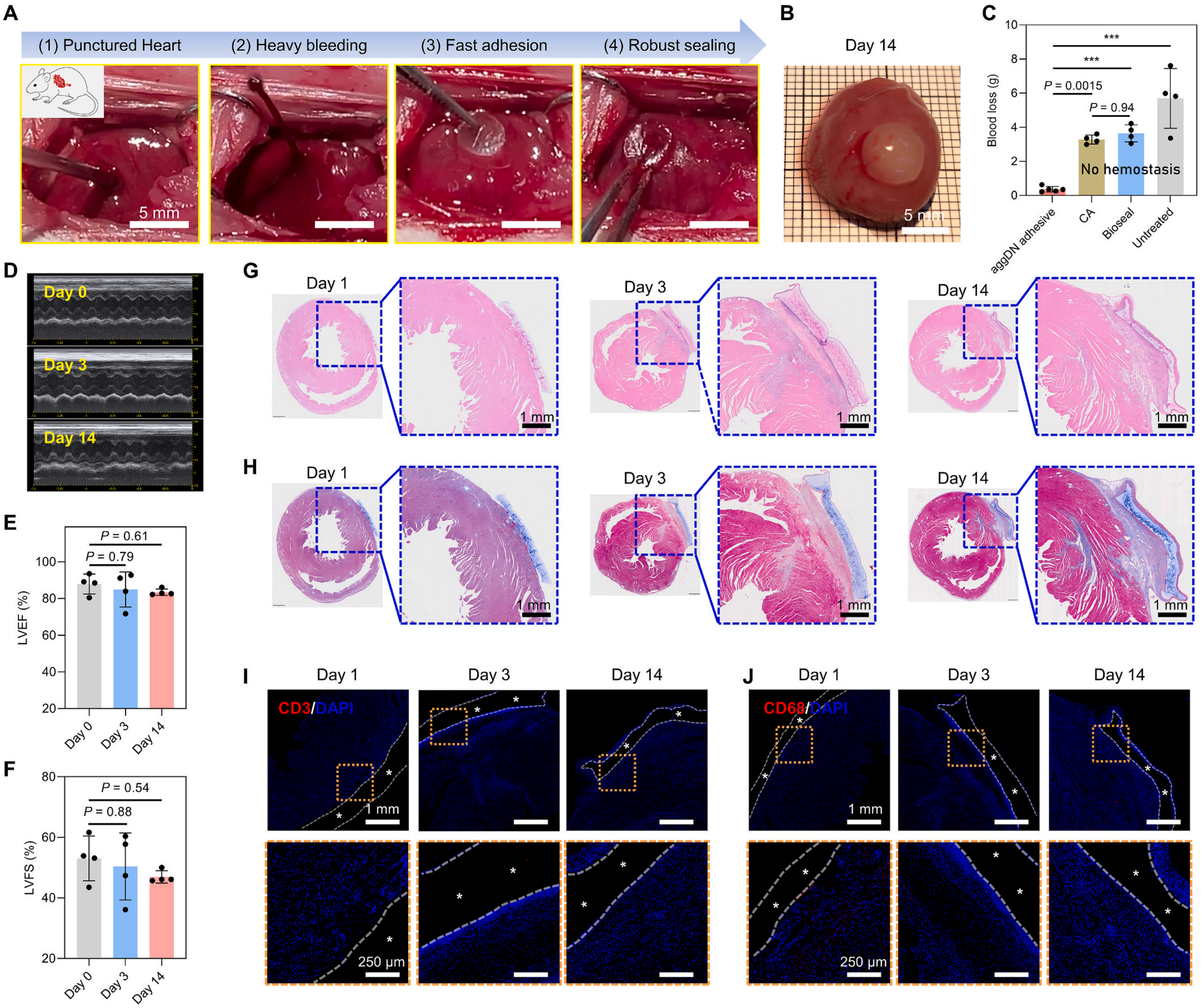

Fig. 6. In vivo evaluation of the sealing capacity for rat heart. (A) Application of the aggDN adhesive hydrogel for the hemostatic sealing of cardiac puncture lesion in rats. (B) Photograph of an aggDN adhesive-sealed rat heart excised at post-operative day 14. (C) Quantification of blood loss until hemostasis for punctured heart treated with aggDN adhesive hydrogel, CA, Bioseal, and control (untreated) (n = 4). The CA, Bioseal, and control groups failed to achieve hemostasis of heart injury in 5 min (D–F) Representative M-mode echocardiographic images (D) and echocardiography measurements (E and F) of rat hearts before injury (day 0), and after injury on days 3 and 14 of post-hemostatic sealing by the aggDN adhesive hydrogel. (G,H) Representative histological images of the aggDN adhesive hydrogel with surrounding tissues stained with H&E (G) and Masson's trichrome (H) staining on days 1, 3, and 14 of post-hemostatic sealing. (I,J) Representative immunofluorescence images of the aggDN adhesive hydrogel with surrounding tissues on days 1, 3, and 14 of post-hemostatic sealing. Blue color represents the cell nuclei (DAPI), red color represents the lymphocytes (CD3, I) and macrophages (CD68, J). Within these immunofluorescence images, the asterisk (*) marks the location of the implanted aggDN adhesive hydrogel. Data in C,E,F represent mean ± SD (n = 4∼5 per group). *P* values were determined by one-way ANOVA followed by Tukey's multiple comparison test (****P* ≤ 0.001).

the lesion interface, characterized by infiltration of a few macrophages (CD68$^+$) and no lymphocyte infiltration (CD3$^+$) (Fig. 6I and J). These findings suggest that our treatment effectively reduces inflammation and promotes myocardial recovery post-surgery. Overall, the tough aggDN adhesive hydrogel, which adheres strongly and conforms well to biological tissues, shows promising potential for applications in hemostatic sealing of dynamic or acute tissue bleeding scenarios.

3.6. *In vivo evaluation of the sealing capacity in a canine aorta incision model*

To further demonstrate the sealing efficacy of the aggDN adhesive hydrogel in managing vascular hemorrhage under high pressure, we conducted a canine aorta lesion model (Fig. 7A). Initially, a 5 mm-long incision was made in the aorta along the blood flow direction (Fig. 7B). In the absence of hemostatic treatment, blood rapidly gushed out from the lesion site at high speed (Fig. 7B). Drawing from the high burst pressure exhibited by aggDN-sealed soft tissue in vitro, we proceeded to apply the aggDN adhesive hydrogel for in vivo sealing of the aorta lesion (Fig. 7B). After approximately 30 s of the hemostatic intervention by aggDN adhesive hydrogel, no blood leakage was detected at the restoration of aortic blood flow (Fig. 7B and Supplementary Movie 9). Notably, widely used clinical adhesives such as Bioseal and CA proved ineffective in promptly arresting the profuse bleeding within a minute (Fig. 7C, D and Supplementary Movie 10). Long-term patency of the sealed aorta was assessed by vascular ultrasonography. Color doppler

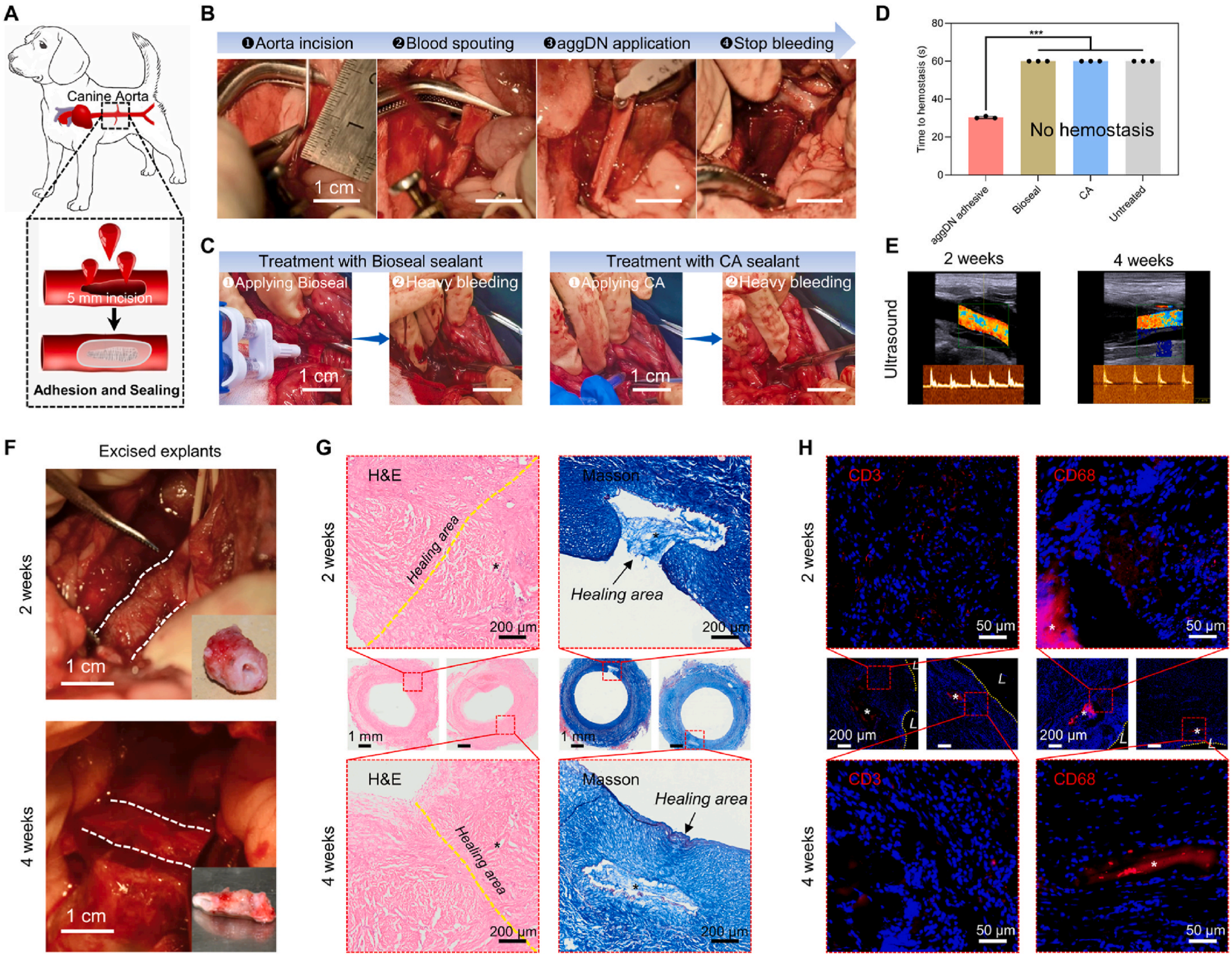

Fig. 7. In vivo evaluation of the sealing capacity for canine aorta. (A) Schematic illustration of hemostatic sealing of canine aorta incision by the aggDN adhesive hydrogel. (B) The sealing process for a canine aorta with a 5-mm-long incision in vivo by the aggDN adhesive hydrogel. (C) The hemostatic sealing for a canine aorta with a 5-mm-long incision in vivo by the clinically used Bioseal and CA sealants. The results indicate that both Bioseal and CA sealants were unable to achieve hemostasis. (D) Time to hemostasis for canine aorta bleeding treated with aggDN adhesive hydrogel, Bioseal, CA, and control (untreated) (n = 3). (E) Representative doppler images of canine aortic blood flow on days 14 and 28 of post-hemostatic sealing by aggDN adhesive hydrogel. (F) Photographs of aggDN adhesive hydrogel-sealed canine aorta excised at post-operative days 14 and 28. (G) Representative histological images of the aggDN adhesive hydrogel with surrounding tissues stained with H&E (left) and Masson's trichrome (right) staining on days 14 and 28 of post-hemostatic sealing. (H) Representative immunofluorescence images of the aggDN adhesive hydrogel with surrounding tissues on days 14 and 28 of post-hemostatic sealing. Blue color represents the cell nuclei (DAPI), red color represents the lymphocytes (CD3, left) and macrophages (CD68, right). Within these images in G and H, the asterisk (*) marks the location of the implanted aggDN adhesive hydrogel and the "*L*" marks the lumen of aorta. Data in D represent mean ± SD (n = 3 per group). *P* values were determined by one-way ANOVA followed by Tukey's multiple comparison test (****P* ≤ 0.001).

images showed that the sealed aorta kept patent evidently post-operation at 2 and 4 weeks (Fig. 7E).

We further evaluated the wound healing of aorta by histological analysis of the aggDN-sealed region excised at postoperative 2 and 4 weeks (Fig. 7F and G). H&E staining indicated the formation of new fibrous tissue in the incision area of aorta, and a little degree of inflammatory response appeared at the lesion site at 2 weeks but nearly disappeared at 4 weeks (Fig. 7G). Masson staining showed that the intima structure of the aorta remained basically intact except for a small notch at the lesion site at 2 weeks (Fig. 7G, up). With the gradual degradation of aggDN, the notch was repaired at 4 weeks (Fig. 7G, down). The integrity of the endothelium also contributed to the absence of thrombosis post-operation (Supplementary Fig. 22). Immunofluorescence staining of CD3 (lymphocytes marker) and CD68 (macrophages marker) were further performed to evaluate the immune response around the sealing region (Fig. 7H). The results showed that aggDN adhesive hydrogel induced tiny inflammatory and foreign-body responses at 2 and 4 weeks. It can also be found that the aggDN adhesive hydrogels were gradually degraded under the resorption of macrophages at 4 weeks. The above results indicates that aggDN adhesive hydrogels have excellent sealing ability for rapid hemostasis and suitable reforming capacity for the repair of soft tissues.

4. Conclusion

In summary, we have developed a tough adhesive hydrogel featuring a bioinspired, hierarchical porous matrix and a bridging polymer for instant and robust tissue adhesion. First, by mimicking the phase separation-assisted aggregation found in natural chromatin, we introduced an external hydrogen bonding element (PLL) to induce the in-situ formation of dispersed microphase aggregates within the pHEAA/agar DN hydrogel. This process effectively remodeled the rigid agar-agar network within the DN hydrogel, resulting in an aggDN matrix with tissue-conformable flexibility and high toughness. Second, we synergistically integrated the aggDN matrix with a pre-activated bridging polymer (HA-NHS) to construct the aggDN adhesive hydrogel. In vitro experiments demonstrated its excellent adhesion and sealing capabilities to various wet tissues, outperforming clinically available bioadhesives. In vivo subcutaneous implantation further validated its biocompatibility and biodegradability. Finally, we further validated the hemostatic sealing capacity of aggDNs in rat models of cardiac hemorrhage and canine models of high-pressure abdominal aorta laceration. The aggDN adhesive hydrogels provide a promising framework for rapid sealing of uncontrollable high-pressure hemorrhagic wound in emergency situations. The fabrication and adhesion mechanism could be applied to design ultrastrong tissue adhesives in more complex scenarios.

CRediT authorship contribution statement

Yinghao Li: Writing – review & editing, Writing – original draft, Methodology, Investigation, Funding acquisition, Conceptualization. **Dongling Xiao:** Writing – original draft, Methodology, Investigation, Data curation. **Weixi Yan:** Investigation, Data curation. **Meilin Jiang:** Investigation, Data curation. **Ju Tan:** Methodology, Investigation. **Zhongliang Qin:** Methodology, Investigation. **Jingting Zhou:** Methodology, Investigation. **Yue Sun:** Methodology, Investigation. **Mingcan Yang:** Investigation. **Guanyuan Yang:** Investigation. **Yawei Gu:** Investigation. **Yong Liu:** Investigation. **Chuhong Zhu:** Writing – review & editing, Supervision, Funding acquisition, Conceptualization.

Ethics approval and consent to participate

All animal experiments were conducted in compliance with ethical regulations for research involving animals and were approved by the Ethics Committee of the Third Military Medical University, China.

Data availability

All data supporting the findings of this study are available within the main text and its Supplementary Information. All other data are available from the corresponding author upon reasonable request.

Declaration of competing interest

Zhongliang Qin and Yong Liu are currently employed by Chongqing Jiukang Medical Research Institute Co., Ltd. The authors declare that they have no known competing financial interests or personal relationships that could have appeared to influence the work reported in this paper.

Acknowledgements

The authors would like to thank J. Sun. H. Zou, and F. Zheng (Third Military Medical University) for help with the in vivo experiments. We would also like to thank Y. Tan (Chongqing Jiukang Medical Research Institute Co., Ltd.) for help with the in vitro experiments. This research was financially supported by the Key project of the National Natural Science Foundation of China (81830055), Youth Project of the National Natural Science Foundation of China (32000966), National Science Fund for Distinguished Young Scholars (31625011), Natural Science Foundation of Chongqing (CSTB2024NSCQ-MSX0606), the Key project of the National Natural Science Foundation of China (82230073), Outstanding Scientist Project of Chongqing (cstc2022ycjh-bgzxm0186) and Frontier Interdisciplinary Research Project of the Army Medical University (2019JCZX06).

Appendix A. Supplementary data

Supplementary data to this article can be found online at https://doi.org/10.1016/j.bioactmat.2024.11.003.

References

[1] B. Guo, R. Dong, Y. Liang, M. Li, Haemostatic materials for wound healing applications, Nat. Rev. Chem 5 (2021) 773–791.
[2] A.M. Behrens, M.J. Sikorski, P. Kofinas, Hemostatic strategies for traumatic and surgical bleeding, J. Biomed. Mater. Res. A 102 (2014) 4182–4194.
[3] D. Reddy, D.J.J. Muckart, Holes in the heart: an atlas of intracardiac injuries following penetrating trauma, Interact. Cardiovasc. Thorac. Surg. 19 (2014) 56–63.
[4] H. Fan, J.P. Gong, Bioinspired underwater adhesives, Adv. Mater. 33 (2021) e2102983.
[5] N. Annabi, et al., Engineering a highly elastic human protein-based sealant for surgical applications, Sci. Transl. Med. 9 (2017) eaai7466.
[6] Y.Z. Bu, A. Pandit, Cohesion mechanisms for bioadhesives, Bioact. Mater. 13 (2022) 105–118.
[7] N. Lang, et al., A blood-resistant surgical glue for minimally invasive repair of vessels and heart defects, Sci. Transl. Med. 6 (2014) 218ra216.
[8] Y. Hong, et al., A strongly adhesive hemostatic hydrogel for the repair of arterial and heart bleeds, Nat. Commun. 10 (2019) 2060.
[9] S.O. Blacklow, et al., Bioinspired mechanically active adhesive dressings to accelerate wound closure, Sci. Adv. 5 (2019) eaaw3963.
[10] E. Shirzaei Sani, et al., Sutureless repair of corneal injuries using naturally derived bioadhesive hydrogels, Sci. Adv. 5 (2019) eaav1281.
[11] J. Saiz-Poseu, J. Mancebo-Aracil, F. Nador, F. Busque, D. Ruiz-Molina, The chemistry behind catechol-based adhesion, Angew. Chem. Int. Ed. 58 (2019) 696–714.
[12] D. Gan, et al., Plant-inspired adhesive and tough hydrogel based on Ag-Lignin nanoparticles-triggered dynamic redox catechol chemistry, Nat. Commun. 10 (2019) 1487.
[13] X. Xu, et al., Bioadhesive hydrogels demonstrating pH-independent and ultrafast gelation promote gastric ulcer healing in pigs, Sci. Transl. Med. 12 (2020) eaba8014.
[14] B. Xu, et al., Hydrogel tapes for fault-tolerant strong wet adhesion, Nat. Commun. 12 (2021) 7156.
[15] C. Cui, et al., Water-triggered hyperbranched polymer universal adhesives: from strong underwater adhesion to rapid sealing hemostasis, Adv. Mater. 31 (2019) 1905761.
[16] J. Li, et al., Tough adhesives for diverse wet surfaces, Science 357 (2017) 378–381.
[17] B.R. Freedman, et al., Enhanced tendon healing by a tough hydrogel with an adhesive side and high drug-loading capacity, Nat. Biomed. Eng. 6 (2022) 1167–1179.
[18] G. Bao, et al., Liquid-infused microstructured bioadhesives halt non-compressible hemorrhage, Nat. Commun. 13 (2022) 5035.
[19] Z. Ma, et al., Controlled tough bioadhesion mediated by ultrasound, Science 377 (2022) 751–755.
[20] B. Guo, Y. Liang, R. Dong, Physical dynamic double-network hydrogels as dressings to facilitate tissue repair, Nat. Protoc. 18 (2023) 3322–3354.
[21] X. Chen, H. Yuk, J. Wu, C.S. Nabzdyk, X. Zhao, Instant tough bioadhesive with triggerable benign detachment, Proc. Natl. Acad. Sci. U.S.A. 117 (2020) 15497–15503.
[22] H. Yuk, et al., Dry double-sided tape for adhesion of wet tissues and devices, Nature 575 (2019) 169–174.
[23] J. Wu, et al., An off-the-shelf bioadhesive patch for sutureless repair of gastrointestinal defects, Sci. Transl. Med. 14 (2022) eabh2857.
[24] G.M. Taboada, et al., Overcoming the translational barriers of tissue adhesives, Nat. Rev. Mater. 5 (2020) 310–329.
[25] Z. Ma, G. Bao, J. Li, Multifaceted design and emerging applications of tissue adhesives, Adv. Mater. 33 (2021) e2007663.
[26] T. Priemel, et al., Microfluidic-like fabrication of metal ion-cured bioadhesives by mussels, Science 374 (2021) 206–211.
[27] G.P. Maier, M.V. Rapp, J.H. Waite, J.N. Israelachvili, A. Butler, Adaptive synergy between catechol and lysine promotes wet adhesion by surface salt displacement, Science 349 (2015) 628–632.
[28] H. Lee, B.P. Lee, P.B. Messersmith, A reversible wet/dry adhesive inspired by mussels and geckos, Nature 448 (2007) 338–341.
[29] D. Zhang, et al., A sandcastle worm-inspired strategy to functionalize wet hydrogels, Nat. Commun. 12 (2021) 6331.
[30] D.-M. Drotlef, et al., Insights into the adhesive mechanisms of tree frogs using artificial mimics, Adv. Funct. Mater. 23 (2013) 1137–1146.
[31] Y. Wang, et al., Water as a "glue": elasticity-enhanced wet attachment of biomimetic microcup structures, Sci. Adv. 8 (2022) eabm9341.
[32] J. Deng, et al., A bioinspired medical adhesive derived from skin secretion of Andrias davidianus for wound healing, Adv. Funct. Mater. 29 (2019) 1809110.
[33] Y. Liu, et al., Underwater instant adhesion mechanism of self-assembled amphiphilic hemostatic granular hydrogel from Andrias davidianus skin secretion, iScience 25 (2022) 105106.
[34] H. Yuk, et al., Rapid and coagulation-independent haemostatic sealing by a paste inspired by barnacle glue, Nat. Biomed. Eng. 5 (2021) 1131–1142.
[35] Y. Liu, et al., Gelation of highly entangled hydrophobic macromolecular fluid for ultrastrong underwater in situ fast tissue adhesion, Sci. Adv. 8 (2022) eabm9744.

[36] H.J. Zhang, et al., Tough physical double-network hydrogels based on amphiphilic triblock copolymers, Adv. Mater. 28 (2016) 4884–4890.

[37] K. Cui, et al., Phase separation behavior in tough and self-healing polyampholyte hydrogels, Macromolecules 53 (2020) 5116–5126.

[38] T.L. Sun, et al., Physical hydrogels composed of polyampholytes demonstrate high toughness and viscoelasticity, Nat. Mater. 12 (2013) 932–937.

[39] X. Li, et al., Mesoscale bicontinuous networks in self-healing hydrogels delay fatigue fracture, Proc. Natl. Acad. Sci. U.S.A. 117 (2020) 7606–7612.

[40] I. Jeon, J. Cui, W.R. Illeperuma, J. Aizenberg, J.J. Vlassak, Extremely stretchable and fast self-healing hydrogels, Adv. Mater. 28 (2016) 4678–4683.

[41] M.T.I. Mredha, et al., A facile method to fabricate anisotropic hydrogels with perfectly aligned hierarchical fibrous structures, Adv. Mater. 30 (2018) 1704937.

[42] M.T. Hua, et al., Strong tough hydrogels via the synergy of freeze-casting and salting out, Nature 590 (2021) 594–599.

[43] Y. Shin, C.P. Brangwynne, Liquid phase condensation in cell physiology and disease, Science 357 (2017) eaaf4382.

[44] S. Alberti, A. Gladfelter, T. Mittag, Considerations and challenges in studying liquid-liquid phase separation and biomolecular condensates, Cell 176 (2019) 419–434.

[45] D.S.W. Lee, N.S. Wingreen, C.P. Brangwynne, Chromatin mechanics dictates subdiffusion and coarsening dynamics of embedded condensates, Nat. Phys. 17 (2021) 531–538.

[46] H. Strickfaden, et al., Condensed chromatin behaves like a solid on the mesoscale in vitro and in living cells, Cell 183 (2020) 1772–1784.

[47] H. Chen, et al., Super bulk and interfacial toughness of physically crosslinked double-network hydrogels, Adv. Funct. Mater. 27 (2017) 1703086.

[48] C.Y. Chang, et al., Hyaluronic acid-human blood hydrogels for stem cell transplantation, Biomaterials 33 (2012) 8026–8033.

[49] S. Kubo, J.F. Kadla, Hydrogen bonding in lignin: a Fourier transform infrared model compound study, Biomacromolecules 6 (2005) 2815–2821.

[50] Y. Uraki, et al., Thermal mobility of β-O-4-type artificial lignin, Biomacromolecules 13 (2012) 867–872.

[51] S. Nitta, M. Akagi, H. Iwamoto, A porous chitosan nanofiber-poly(ethylene glycol) diacrylate hydrogel for metal adsorption from aqueous solutions, Polym. J. 51 (2019) 501–509.

[52] B. Babaei, A. Davarian, K.M. Pryse, E.L. Elson, G.M. Genin, Efficient and optimized identification of generalized Maxwell viscoelastic relaxation spectra, J. Mech. Behav. Biomed. Mater. 55 (2016) 32–41.